# 2. GUIDING-CENTER MOTION IN TOKAMAKS

Basic studies of neoclassical transport have been done by a number of workers [14-18]. These papers, as well as in Chapters 2-7 of this work, make seven basic assumptions: 1) the tokamak fields are axisymmetric, i.e. magnetic field ripple is neglected; 2) the particle gyroradius, $r_g$, is much smaller than the scale size of the magnetic field; 3) diamagnetic effects due to finite plasma pressure are negligible; 4) the plasma is collisionless, implying that no slowing down or pitch angle scattering occurs during one banana orbit; 5) the toroidal current density is a function of poloidal radius only; 6) the toroidal magnetic field is much larger than the poloidal field; 7) electric field effects on the orbits are negligible. Petrie [19-21] has analyzed the electric field effects due to fusion-product losses. His results show that the resulting $\vec{E} \times \vec{B}$ drift does not affect the fusion-product orbits, and that electrical potential ($\Phi$) retardation of fusion-product losses is negligible, i.e. $e\Phi \lesssim kT << E$.

## 2.1 Previous Work

Prior work has concentrated on plasma transport [1] and gross features of high-energy ion losses[6,15-18]. The present work is the first to calculate wall loading fluxes [101]. In developing the techniques for this calculation, modifications and generalizations of the theory

were necessary. In particular, this work eliminates the small banana width approximation of Galeev and Sagdeev [14], and excludes the numerical procedures of Stringer [15], McAlees [16], Tenney [17] and Ohnishi et al. [6]. The latter methods require much computer time and would be difficult to extend to wall loading calculations. Rome et al. [18] calculate the velocity-space loss region for injected ions, but do not apply their results to compute wall loading. Specifically, they extend McAlees' work to analytically determine the pitch angle corresponding to the orbit tangent to a limiter at r = a (the toroidal coordinates are defined in Fig. 2.1), and also derive an expression to numerically compute the pitch angle for the "fattest" banana orbit. Their results hold only for particles born in the equatorial plane with $R > R_0$. To extend the loss analysis over the whole plasma, Rome et al. note that the orbit equation can be used to map other points unto the corresponding points for z = 0, $R \geq R_0$; however, as they point out, this procedure is tedious in practice.

## 2.2 Large Banana-Width Orbits

The present study employs a more general analytic formulation to calculate orbits incident on a limiter at r = a and/or a wall at r > a, from an arbitrary birth point. Our loss region algorithm extends that of Ref. 18 to include the effects of stagnation-orbits for $R > R_0$, orbits grazingly incident on the wall in the mid-plane for $R < R_0$ and also grazingly incident on the wall out of the mid-plane, $\chi = 0$ orbits for $R > R_0$, and elimination of disconnected orbits from the set of valid solutions (see Chapter 3). These effects are especially

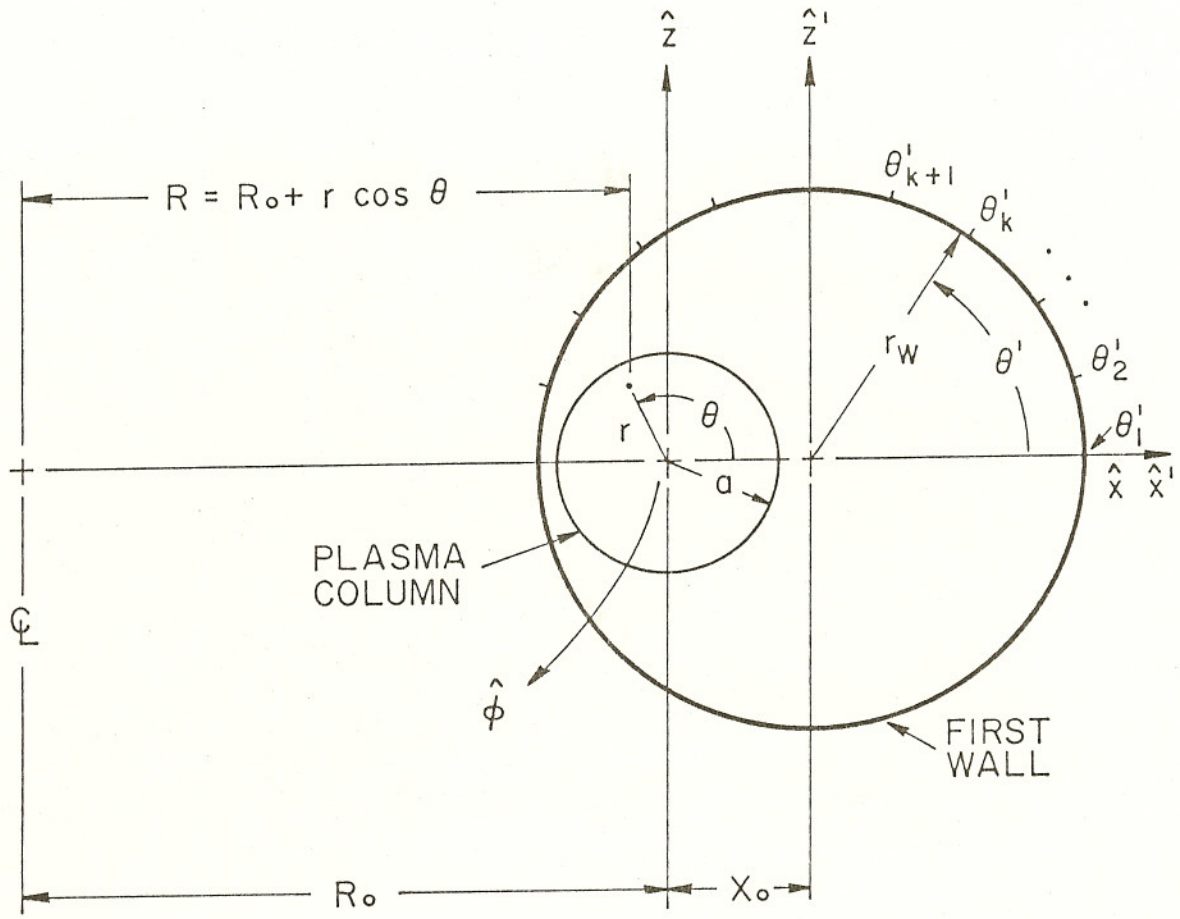


Figure 2.1 The toroidal coordinate geometry is shown here with $\hat{\phi}$ in the toroidal direction. The origin of the primed coordinates is located at the center of the wall cross section.

important for high-energy fusion products (E > 1 MeV) with birth points near the plasma edge (e.g. ORNL-EPR and UWMAK I) and can introduce errors > 10% in loss fraction (see Chapter 4).

The basic properties of banana orbits have been reviewed by Kadomstev and Pogutse [22], and will not be repeated here. Under the assumptions stated at the beginning of this chapter, the Lagrangian of motion for a particle of mass, m, and charge, Ze, is:

$$L = \frac{m}{2}(\dot{r}^2+r^2\dot{\theta}^2+R^2\dot{\phi}^2) + Ze(\dot{r}A_r+r\dot{\theta}A_\theta+R\dot{\phi}A_\phi), \tag{2.1}$$

where electric fields are assumed to be negligible. From the axisymmetry condition, $\partial L/\partial\phi = 0$, together with $B_\theta << B_\phi$, the well-known canonical angular momentum is obtained: $P_\phi = mR_o hv_\parallel + ZeR_o hA_\phi$

where $h = R/R_o$, $v_\parallel = v\cos\chi$, and $\chi$ = the angle between $\vec{v}$ and $\vec{B}$. From the $\theta$-component of $\vec{B} = \nabla \times \vec{A}$, one obtains $hA_\phi = -\int_o^r B_\theta(r)dr$, where the Knorr form [23] for the magnetic field is used: $\vec{B} = h^{-1}(\hat{\theta}B_\theta(r) + \hat{\phi}B_o)$, $B_o$ = constant. The resulting expression for $P_\phi$ is:

$$P_\phi = mR_o hv_\parallel - Ze\psi \tag{2.2}$$

where $\psi = R_o \int_o^r B_\theta(r)dr$. Assuming a toroidal electric-current density of the form

$$J = J_o\left[1 - \gamma\left(\frac{r}{a}\right)^N\right]^M, \tag{2.3}$$

the following expression for poloidal flux function, $\psi(r)$, is obtained with N real and M a positive integer:

$$\psi(r) = \begin{cases} \dfrac{\mu_o I R_o}{2\pi} \displaystyle\sum_{j=0}^{M} \frac{(-\gamma)^j (r/a)^{jN+2}}{j!(M-j)!(jN+2)^2} \Big/ \sum_{j=0}^{M} \frac{(-\gamma)^j}{j!(M-j)!(jN+2)}, & r \leq a \quad (2.4) \\ \dfrac{\mu_o I R_o}{2\pi} \left[ \ell n \dfrac{r}{a} + \displaystyle\sum_{j=0}^{M} \frac{(-\gamma)^j}{j!(M-j)!(jN+2)^2} \Big/ \sum_{j=0}^{M} \frac{(-\gamma)^j}{j!(M-j)!(jN+2)} \right], & r \geq a \quad (2.5) \end{cases}$$

where these equations are in rationalized mks units.

To obtain the equation of motion, the invariants $\mu = W_\perp/B$ and $E = W_\perp + \frac{1}{2} m v_\parallel^2$ are combined to obtain $v_\parallel = \pm \sqrt{2(E-\mu B_o/h)/m}$. As first done by Meka [24], this last expression is then substituted into (2.2) to obtain the orbital equation:

$$\left.\begin{aligned} x &= R_o[\tfrac{1}{2} h_i \sin^2 \chi_i + \tfrac{1}{2} \sqrt{h_i^2 \sin^4 \chi_i + 4(P_\phi + Ze\psi(r))^2/(mvR_o)^2} - 1], \\ z &= \pm \sqrt{r^2 - x^2}, \end{aligned}\right\} \quad (2.6)$$

where the subscript "i" refers to the initial point of the orbit. Equation (2.6) is the projection of the particle guiding center motion onto the x-z plane (see Fig. 2.1), and arises from toroidal axisymmetry (i.e. the $\phi$-coordinate is ignorable.) It provides an especially convenient, analytical expression for generating and analyzing particle orbits.

Two useful properties of this orbital equation should be noted. First, express (2.6) as an equation for $x = x(r, \chi_i, B_\phi, B_\theta)$. Then from (2.2) and (2.4)-(2.5), the symmetries with respect to the last three variables are obtained; namely:

$$x(r,\chi_i,B_\phi,B_\theta) = \begin{cases} x(r,\pi-\chi_i,-B_\phi,B_\theta) & (2.7a) \\ x(r,\pi-\chi_i,B_\phi,-B_\theta) & (2.7b) \\ x(r,\chi_i,-B_\phi,-B_\theta) & (2.7c) \end{cases}$$

Secondly, consider the ratio of $\psi/mvR_o$ for two different particles at a given poloidal radius and identical reactor parameters. From (2.4)-(2.5), we find:

$$\frac{\psi_1/m_1v_1R_o}{\psi_2/m_2v_2R_o} = \frac{Z_1}{Z_2}\sqrt{\frac{m_2E_2}{m_1E_1}} = \frac{Z_1}{Z_2}\frac{P_2}{P_1} \qquad (2.8)$$

where $P_i$ is the particle momentum. Combining (2.8) and (2.6) implies that identical orbits result when,

$$(Z_1/Z_2)(P_2/P_1) = 1. \qquad (2.9)$$

Thus, identical fusion product orbits occur for two equally charged fusion products from the same reaction (e.g. for T and P from D(d,p)T), since then $P_1 = P_2$. Another consequence of this last condition is that protons and alphas of the same energy have essentially the same orbits. These properties will be used in Chapter 4, in discussing wall-loading profiles for various fusion products.

To calculate the loss region in velocity space, it is necessary to study the drift orbit properties. Figures 2.2 and 2.3 show orbits for D-$He^3$ fusion products (3.7-MeV $\alpha$ and 14.7-MeV p) in the TFTR weak compression (TFTR I) plasma (see Table 2.1 for machine parameters). D-$He^3$ is of interest because it avoids neutron- and tritium-radiation

Table 2.1: Tokamak Parameters

| Machine | PLT[26]** | TFTR I[27]+ | TFTR II[27] | ORNL-EPR[28]† | UWMAK I[29]@ |
|---|---|---|---|---|---|
| $B_o$(T) | 4.6 | 5.2 | 5.2 | 4.8 | 3.82 |
| I(MA) | 1 | 1 | 2.5 | 7.2 | 21 |
| $R_o$(m) | 1.32 | 2.48 | 2.48 | 6.75 | 13.00 |
| a(m) | 0.45 | 0.54 | 0.85 | 2.25 | 5.00 |
| $r_w$(m) | 0.48 | 1.10 | 1.10 | 2.25 | 5.50 |
| $X_o$(m) | 0 | 0.17 | 0.17 | 0 | 0 |
| $T_{io}$(keV) | 5 | 10 | 10 | 22.5* | 11.1 |
| $T_i/T_{io}$ | $1-.8(r/a)^2$ | $1-.8(r/a)^2$ | $1-.8(r/a)^2$ | $1-(r/a)^2$ | 1 |
| $n_{io}(m^{-3})$ | $1x10^{20}$ | $1.6x10^{20}$ | $1.6x10^{20}$ | $8x10^{19}$ | $1.2x10^{20}$ |
| $n_i/n_{io}$ | $1-(r/a)^2$ | $1-(r/a)^2$ | $1-(r/a)^2$ | $[1-(r/a)^2]^{\frac{1}{2}}$ | $[1-.99(r/a)^2]^{\frac{1}{2}}$ |
| $J/J_o$ | $1-(r/a)^2$ | $1-(r/a)^2$ | $1-(r/a)^2$ | $1-(r/a)^2$ | 1 |
| q(a) | 3.53 | 3.06 | 3.03 | 2.50 | 1.75 |

*An ignited system is assumed, having a thermal power of 420 MW.

**Princeton Large Torus

+Tokamak Fusion Test Reactor

†Oak Ridge National Laboratory-Engineering Power Reactor

@University of Wisconsin TokaMAK-Deisgn I

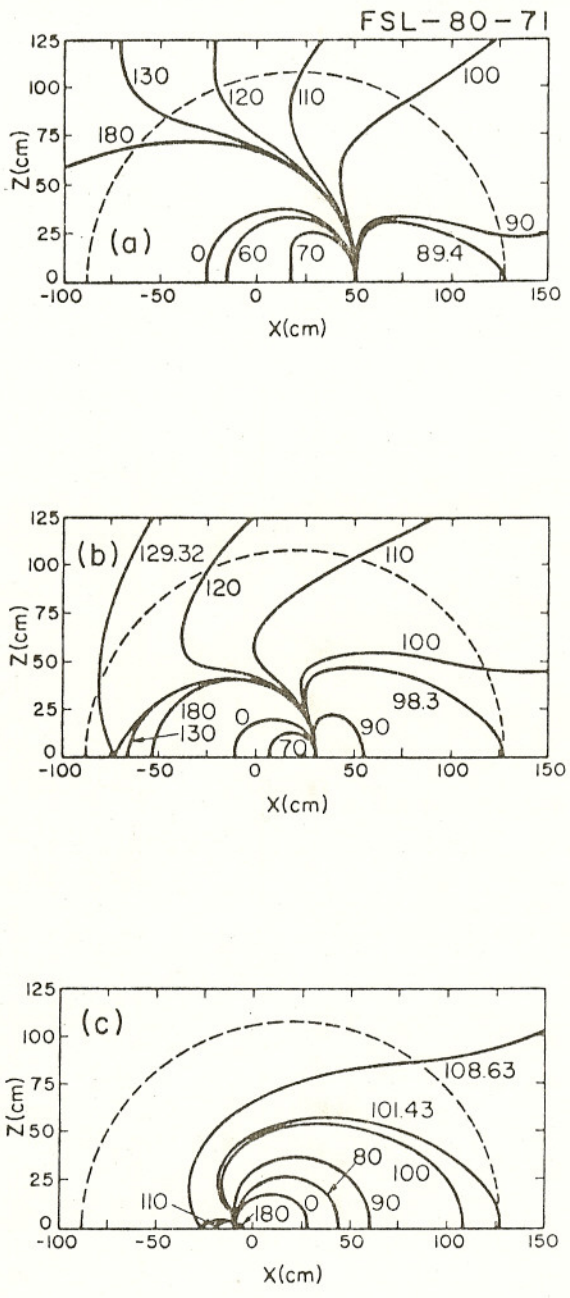


Figure 2.2 Neoclassical guiding-center orbits of a 3.7-MeV $\alpha$, for various birth points on the x-axis (50,30,-10 cm) in the TFTR weak compression plasma. The origin is positioned at the plasma column center ($R_0$ = 248 cm, a = 54 cm). The dashed semi-circle in each graph indicates the first wall position ($r_W$ = 110 cm, $X_0$ = 17 cm). The number on each curve is the pitch angle at birth.

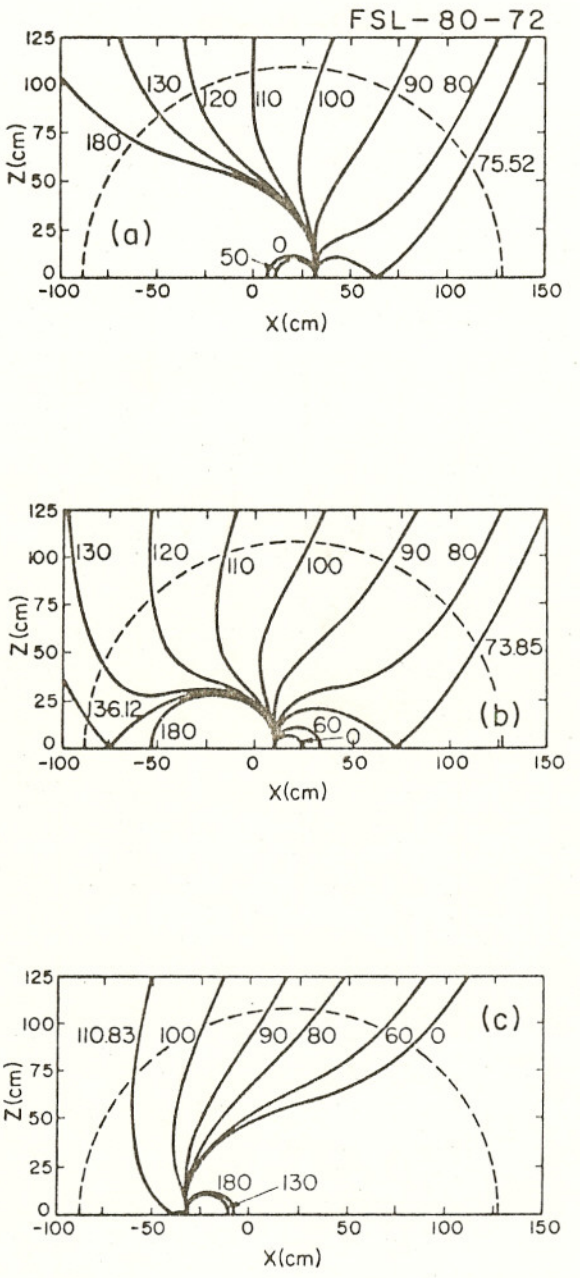


Figure 2.3 Neoclassical guiding-center orbits of a 14.7-MeV p, for various birth points on the x-axis (30,10,-30 cm) in the TFTR weak compression plasma. The origin is positioned at the plasma column center ($R_0$ = 248 cm, a = 54 cm). The number on each curve is the pitch angle at birth.

hazards in proposed fusion-product detection experiments [25]. Simultaneously, the alpha behavior is quite similar to the 3.5-MeV $\alpha$ from D-T. Note that only the $z \geq 0$ half of the orbits are plotted because (2.6) indicates symmetry in $\pm z$. The first wall position is indicated by the dashed line.

The details of the loss boundaries are considered next. For the 3.7-MeV $\alpha$, the lower loss boundary in pitch-angle space, $\chi_{min}$, intersects the wall at grazing incidence. The upper loss boundary, $\chi_{max}$, corresponds to the "fattest" banana in Figs. 2.2b-2.2c, and to $\chi_{max} = 180°$ in Fig. 2.2a. The "fattest" banana is what Tenney [17] calls a stagnation orbit, and the point where this orbit touches the x-axis ($dz/dx = 0$), Tenney terms the stagnation point (Rome, et al. [18] refer to this point as the pinch point). At the stagnation point, $x_s$, the drift motion in $\hat{z}$ slows to zero, then reverses (stagnates) due to cancellation of the motion along the flux surface with the vertical drift (arising from $\nabla B$ and curvature effects). The point, $x_s$, is really an "unstable" stagnation point [30] since the particle takes an infinite time to drift there. This is to be distinguished from a "stable" stagnation point, which also has zero net vertical drift and which corresponds to the "point" orbit discussed in Chapter 3.

Additional features of these orbits are illustrated in Fig. 2.3. Particularly noteworthy are the stagnation orbits which occur for $R > R_o$ (see Figs. 2.3a-3b), caused by the same cancellation of vertical drift with motion along the flux surface. The existence of

unstable stagnation points for both $R < R_o$ and $R > R_o$ is interesting and has been discussed by Goldston [30], who elucidated the features of such orbits for fast, neutral-beam-injected ions in ATC. The $R > R_o$ unstable stagnation orbits for the 14.7-MeV p correspond to the lower loss boundary, $\chi_{min}$. Also, in Fig. 2.3c is an instance in which $\chi_{min} = 0$; and in Fig. 2.3a is a case for which $\chi_{max} = 180°$. Not shown in these figures are a small class of orbits which intersect the wall at grazing incidence for $R < R_o$, corresponding to $\chi_{max}$.

Another feature of the $R < R_o$ stagnation orbits can be seen in the sequence of Figs. 2.2b-2.2c and 2.3b-2.3c: as the major radius of the initial point ($R_i = R_o + x_i$) decreases, the major radius of the unstable stagnation point ($R_s = R_o + x_s$) increases. Consequently, there is a critical position ($R_c^- = R_o + x_c^-$) for which $x_i - x_s \to 0$. This situation corresponds to the orbit loop between the initial and stagnation points shrinking to a point as $x_i \to x_c^-$ for $x_i > x_c^-$. There is an analogous limit for $R > R_o$ stagnation orbits, since for these orbits $R_s$ decreases as $R_i$ increases; the corresponding critical position is $R_c^+ = R_o + x_c^+$. For birth points on the x-axis at $(x_i, 0)$, outside the interval $x_c^- < x_i < x_c^+$, $x_s$ coincides with $x_i$. Although the orbit loop, from birth to stagnation, shrinks to a point in this case, the "fattest banana" portion of the orbit can still carry the fast ion to the wall.

Finally there is a very specialized case of the stagnation orbit, illustrated in Fig. 2.4, for a 3.52-MeV $\alpha$ in TFTR I with $J/J_o = 1-(r/a)^{.01}$.

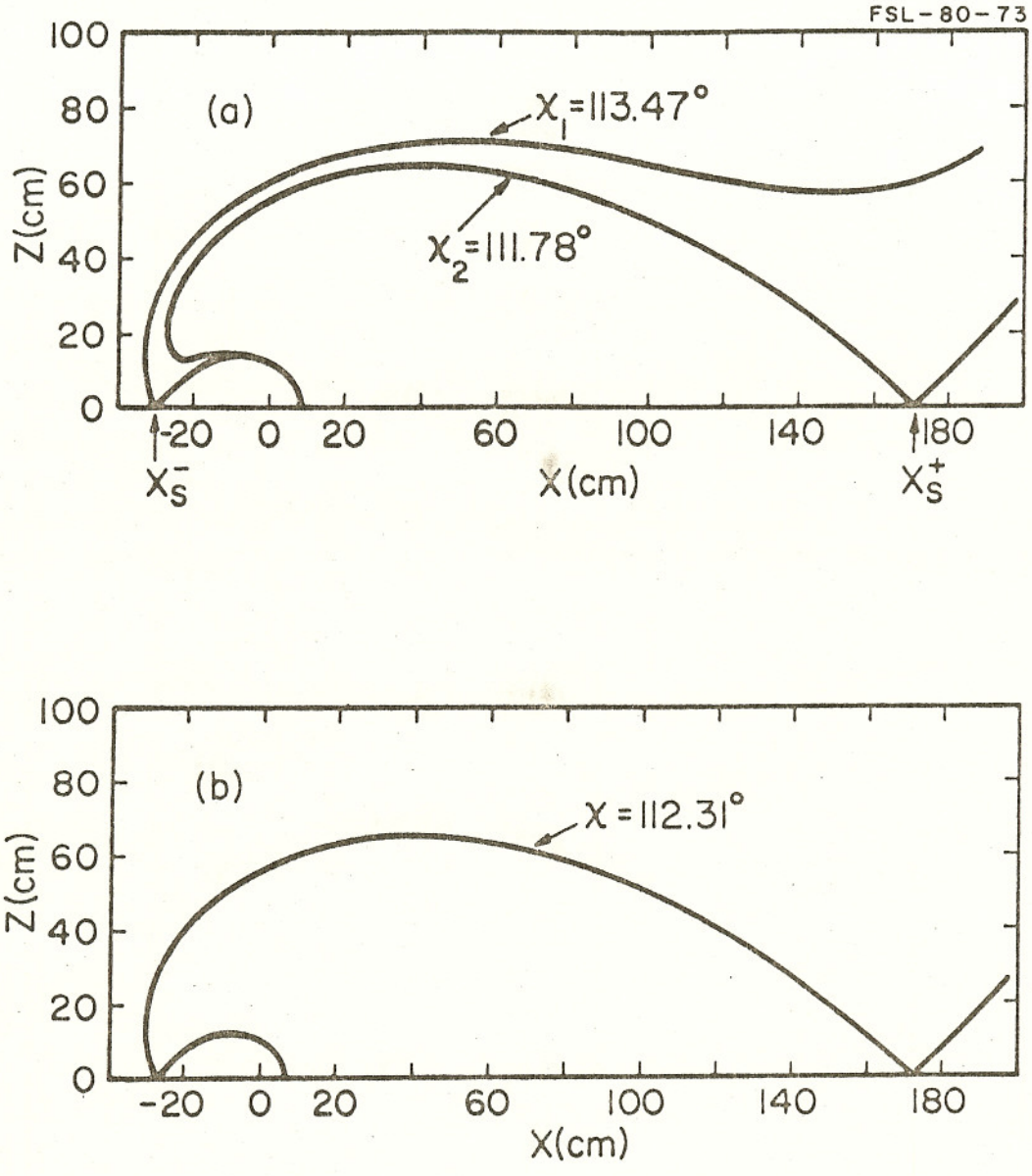


Figure 2.4 Stagnation drift orbits of a 3.52-MeV $\alpha$ in the TFTR-I plasma with $J/J_0 = 1-(r/a)^{.01}$, for birth points on the x-axis at 8 cm (Fig. 2.4a) and 6.34 cm (Fig. 2.4b). A double stagnation orbit is shown in Fig. 2.4b.

In Fig. 2.4a, both the upper and lower loss boundaries are stagnation orbits for a birth point at $x_i$ = 8 cm on the x-axis. As the x-value of the birth point decreases to $x_i$ = 6.34 cm in Fig. 2.4b, the two orbits coalesce into a double stagnation orbit. For $x_i$ < 6.34 cm, the $R < R_0$ stagnation orbit becomes the "fattest" banana, and the $R > R_0$ stagnation orbit becomes a counter-circulating orbit.

Fig. 2.4a suggests an interesting possibility for high-energy ion beam injection [31]. Neutral beam injection can be replaced by ion injection into the spatial and velocity regions bounded by a pair of stagnation orbits, like those of Fig. 2.4a. The ion injectors can be coupled to the tokamak via a bundle divertor. The ions can then enter the plasma along orbits corresponding to $\chi_2 < \chi < \chi_1$. It would be strongly advantageous to inject close to the outer stagnation orbit, $\chi = \chi_1$, for two reasons. First, any ions near the inner stagnation orbit, $\chi = \chi_2$, can easily charge exchange with neutrals near the plasma edge while moving slowly through the outboard stagnation point at $x = x_s^+$. Second, ions near the outer stagnation orbit will spend much time near the inboard stagnation point ($x = x_s^-$), and thus deposit more energy at the plasma core than at the plasma edge. The ions can be trapped in the plasma by pitch-angle scattering near the inboard stagnation point. Ions can also be pitch-angle scattered into loss orbits, but these orbits are well-defined, so lost particles might be recovered and re-injected. Although injection along stagnation orbits is a difficult problem, the advantage of ion injection offers a strong motivation for considering such a technique. While this is an intriguing problem for more study, it will not be discussed further.